Supporting Information

Kasahara et al. 10.1073/pnas.1413477111

SI Text

1. Sample Growth and Characterization

High-quality single crystals of tetragonal β-FeSe were grown by the vapor transport method at Karlsruhe Institute of Technology. (1). A mixture of Fe and Se powders was sealed in an evacuated SiO_2 ampoule together with KCl and $AlCl_3$ powders. The ampoule was heated to 390 °C on one end while the other end was kept at 240 °C. After 28.5 d, single crystals of FeSe with tetragonal morphology were extracted at the cold end. We note that the crystals grow directly in the tetragonal phase at these temperatures, resulting in high-quality single crystals free from structural transformations or decomposition reactions. Wavelength-dispersive X-ray spectroscopy reveals an impurity level below 500 ppm. In particular, there is no evidence of Cl, Si, K, or Al impurities. X-ray diffraction confirms the tetragonal structure with lattice constants $a = 3.7707(12)$ Å and $c = 5.521(3)$ Å. Structural refinement shows the stoichiometric composition of Fe and Se within the error [Fe:Se = 0.995(4):1]. The structural z parameter of Se is $z_{Se} = 0.26668(9)$. No indications for interstitial atoms were found.

The extremely small level of impurities and defects (less than one impurity per 2,000 Fe atoms) are confirmed by scanning tunneling microscope (STM) topography (Fig. S1).

Fig. S2*B* shows the magnetic susceptibility χ of the sample used for the penetration depth measurements (Fig. 1*B*), which is measured by superconducting quantum interference device magnetometer under zero-field cooling condition with a field applied parallel to the c axis ($H = 1$ Oe). The sample size is approximately $300 \times 300 \times 10$ μm^3. The susceptibility shows sharp transition with the width (10–90%) of 0.3 K and T_c defined as the midpoint of the transition as 9.25 K. Fig. S2*A* shows the resistive transition of another sample of the same batch (Fig. 1*A*, *Inset*). The temperature at which the resistivity goes to zero is 9.40 K, which is very close to T_c determined by χ.

The high quality of our samples allows quantum oscillations above H_{irr} to be observed (2). The results, together with large *RRR* value (Fig. 1*A*), large magnetoresistance (Fig. 1*A*, *Inset*), and extremely small level of impurities and defects (Fig. S1), demonstrate that the crystals used in the present study are very clean.

2. Transport Measurements

Thermal conductivity and magnetoresistance were measured on the same crystal ($880 \times 340 \times 10$ μm^3) using the same contacts. We attached the contacts after cleaving the surface. The thermal conductivity was measured by the standard steady-state method in a dilution refrigerator. Hall and Seebeck measurements were performed on another crystal ($850 \times 1000 \times 5$ μm^3).

Above 10 K, the magnetoresistance $\Delta\rho/\rho \equiv (\rho(H) - \rho)/\rho$ exhibits an H^n ($n \sim 2$) dependence without saturation (Fig. S3*A*), which demonstrates the nearly perfect compensation, i.e., an equal density of electrons and holes, $n_h = n_e$. In a compensated metal, the magnetoresistance is given by $\Delta\rho/\rho = (\omega_c^e \tau_e)(\omega_c^h \tau_h)$, where $\omega_c = e\mu H/m$ is the cyclotron frequency for carriers with mass m and scattering time τ (3). The suffixes e and h denote "electron" and "hole," respectively. At $T = 10$ K we estimate $(\omega_c^e \tau_e)(\omega_c^h \tau_h) \approx 5$ at 10 T, indicating the high mobility of charge carriers.

Fig. S3*B* shows the temperature dependence of the Hall coefficient R_h in the zero-field limit. Above 100 K, R_h is close to zero. Below ~60 K, R_h is negative and strongly temperature dependent. In a compensated metal, the Hall coefficient is given by $R_h = 1/n_e e((\omega_c^e \tau_e - \omega_c^h \tau_h)/(\omega_c^e \tau_e + \omega_c^h \tau_h))$ (3). The strong T dependence of R_h indicates that the electron and hole mobilities are of the same order (4), which is consistent with the QPI results.

Fig. S3*C* shows the temperature dependence of the Seebeck coefficient divided by T, S/T. Below 40 K, S is negative. The Seebeck coefficient in the single-band case is expected to be T-linear in the zero-temperature limit and linked to ε_F by $S/T = \pm(\pi^2/2)(k_B^2/e)(1/\varepsilon_F)$. In a multiband system with both electrons and holes contributing with opposite signs to the overall Seebeck response, the single-band formula sets an upper limit to the Femi energy of the dominant band (5). From $S/T \sim 3.5$ μV/K^2 at low temperatures above T_c, we estimate the upper limit of ε_F^e to be ~10 meV.

3. London Penetration Depth

To determine the absolute value of the in-plane London penetration depth $\lambda_L(0)$ in a small single crystal reliably, we combined the high-precision tunnel diode oscillator (TDO) (resonant frequency of $f = 13$ MHz) and the microwave cavity perturbation ($f = 28$ GHz) techniques (6).

For the TDO technique, we can determine the change of the London penetration depth $\delta\lambda_L \equiv \lambda_L(T) - \lambda_L(0)$ by the change of the resonant frequency $\delta f \equiv f(T) - f(0)$, $\delta f = G\delta\lambda_L$. The calibration factor G is determined from the geometry of the sample. We measured δf down to 100 mK.

For the microwave cavity perturbation technique, we used a superconducting cavity resonator with high Q factor ($Q > 10^6$). We measured the microwave surface impedance $Z_s = R_s + iX_s$ in the Meissner state down to 4.2 K, where R_s and X_s are the surface resistance and reactance, respectively (Fig. S4*A*). In the present frequency range, the complex conductivity $\sigma = \sigma_1 - i\sigma_2$ in the skin-depth regime is given by Z_s through the relation

$$Z_s = R_s + iX_s = \left(\frac{i\mu_0\omega}{\sigma_1 - i\sigma_2}\right)^{1/2}. \quad [S1]$$

In the Hagen–Rubens limit, $\omega\tau \ll 1$, where ω is the microwave frequency and τ is the scattering rate, σ_2 is related to λ_L by $\sigma_2 = 1/\mu_0\omega\lambda_L^2$. In Fig. S4*B*, the blue circles show $\sigma_2(T)/\sigma_2$ (4.2 K), which represent the normalized superfluid density ρ_s. The solid lines represent ρ_s obtained from $\delta\lambda_L(T)$ assuming several different $\lambda_L(0)$ values. The best fit is obtained for $\lambda_L(0) \approx 400$ nm.

4. Quasiparticle Interference

Fig. S5 *A–L* shows the energy-dependent QPI patterns at 12 T. Fig. S5 *A–C* displays the normalized conductance images of occupied states. To avoid the so-called set-point effect associated with the spatial variation of the integrated density of states (7), raw conductance data dI/dV are normalized by I/V, where I and V are tunneling current and bias voltage, respectively (8). The nearest-neighbor Fe–Fe distance is larger along the b axis than along the a axis. Fig. S5 *D–F* displays Fourier-transformed images of Fig. S5 *A–C*. Fig. S5 *G–I* displays the normalized conductance images of unoccupied states. Fig. S5 *J–L* displays Fourier-transformed images of Fig. S5 *G–I*.

Fig. S6*A* shows STM topographic image of the dumbbell-shaped impurity. Fig. S6*B* shows scanning tunneling spectroscopy (STS) spectra at the impurity (blue) and at the position far from the impurity (red). A sharp peak at +10 meV in the STS spectrum (blue) arises from the impurity bound state, which gives rise to the q-independent dispersion shown in Fig. 2 *B–E*.

5. Magnetic Torque

The magnetic torque was measured using a piezoresistive microcantilever technique down to 30 mK and up to 17.8 T. A small single crystal of approximately $100 \times 100 \times 15$ μm^3 was mounted on the lever with a tiny amount of Apiezon grease. The field is slightly tilted away from the c axis. Fig. S7 shows the field dependence of the torque signal. The irreversibility field H_{irr} is defined by the point where the hysteresis loop has closed to a level of 0.3% (arrows pointing down). We note that H_{irr} determined by the magnetic torque coincides well with the H_{irr} defined by the zero resistivity as shown in Fig. 4 in the main text. A broad peak effect associated with the order–disorder transition of the flux-line lattice is observed after subtraction of a smooth background (arrows pointing up indicate the maximum). The peak field is seen to be strongly temperature dependent, in contrast with the H^* line.

1. Böhmer AE, et al. (2013) Lack of coupling between superconductivity and orthorhombic distortion in stoichiometric single-crystalline FeSe. *Phys Rev B* 87(18):180505(R).
2. Terashima T, et al. (2014) Anomalous Fermi surface in FeSe seen by Shubnikov-de Haas oscillation measurements. *Phys Rev B* 90(14):144517.
3. Pippard AB (1989) *Magnetoresistance in Metals* (Cambridge Univ Press, Cambridge, UK).
4. Kasahara Y, et al. (2007) Exotic superconducting properties in the electron-hole-compensated heavy-fermion "Semimetal" URu_2Si_2. *Phys Rev Lett* 99(11):116402.
5. Pourret A, et al. (2011) Strong correlation and low carrier density in Fe_{1+y} $Te_{0.6}Se_{0.4}$ as seen from its thermoelectric response. *Phys Rev B* 83(2):020504(R).
6. Hashimoto K, et al. (2012) A sharp peak of the zero-temperature penetration depth at optimal composition in $BaFe_2(As_{1-x}P_x)_2$. *Science* 336(6088):1554–1557.
7. Chen CJ (2008) *Introduction to Scanning Tunneling Microscopy* (Oxford Univ Press, Oxford).
8. Feenstra RM, Stroscio JA, Fein AP (1987) Tunneling spectroscopy of the Si(111)2 × 1 surface. *Surf Sci* 181(1-2):295–306.

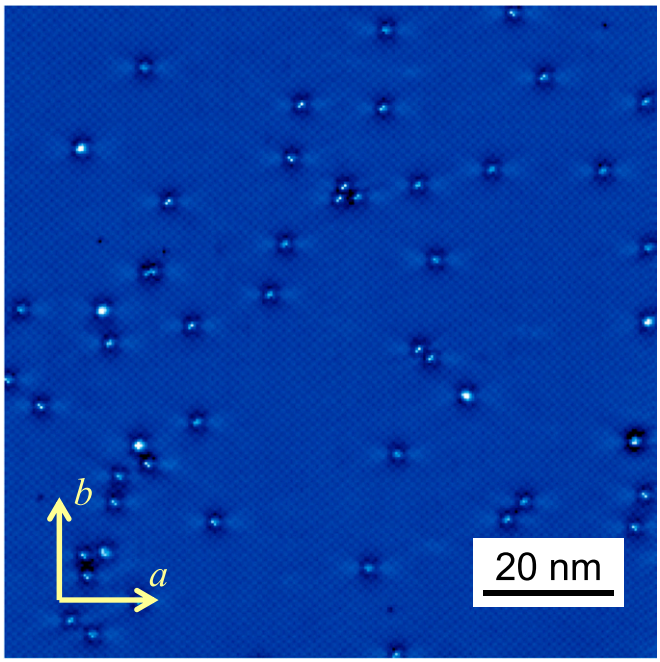

Fig. S1. STM topograph of FeSe at 1.5 K. White bright spots are impurities or defects. Feedback conditions are sample bias voltage $V_s = +95$ mV and tunneling current $I_t = 10$ pA.

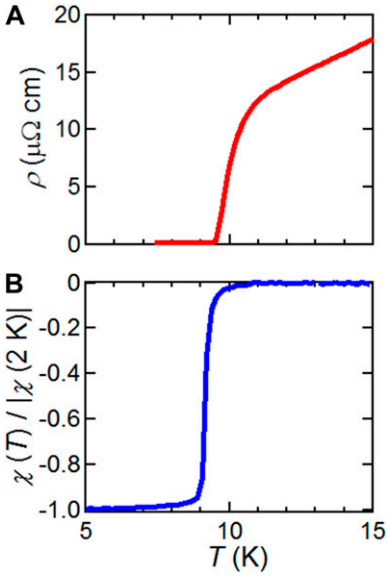

Fig. S2. Superconducting transition of FeSe single crystals. (*A*) Resistive transition in zero field. (*B*) Magnetic susceptibility measured under zero-field cooling condition.

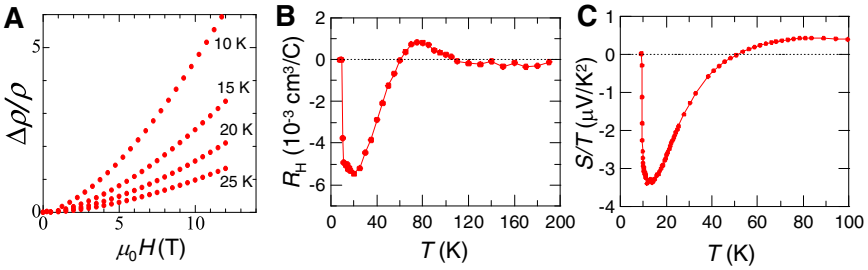

Fig. S3. Transport properties of FeSe single crystals. (*A*) Magnetoresistance above 10 K. (*B*) Temperature dependence of the Hall coefficient R_H. (*C*) Temperature dependence of the Seebeck coefficient divided by T, S/T.

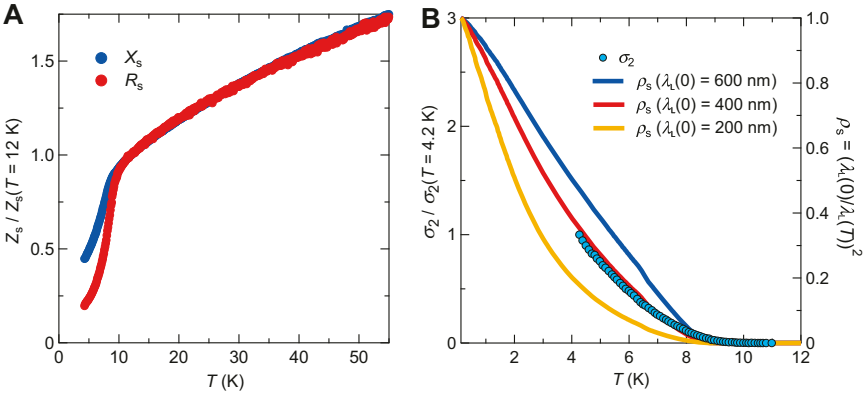

Fig. S4. Determination of absolute value of the penetration depth. (*A*) Temperature dependence of the microwave surface resistance R_s and reactance X_s. (*B*) Temperature dependence of σ_2 in microwave surface impedance measurements (blue circles, right axis) and normalized superfluid density ρ_s calculated from $\delta\lambda_L$ in TDO measurements by assuming different values of $\lambda_L(0)$ (solid lines).

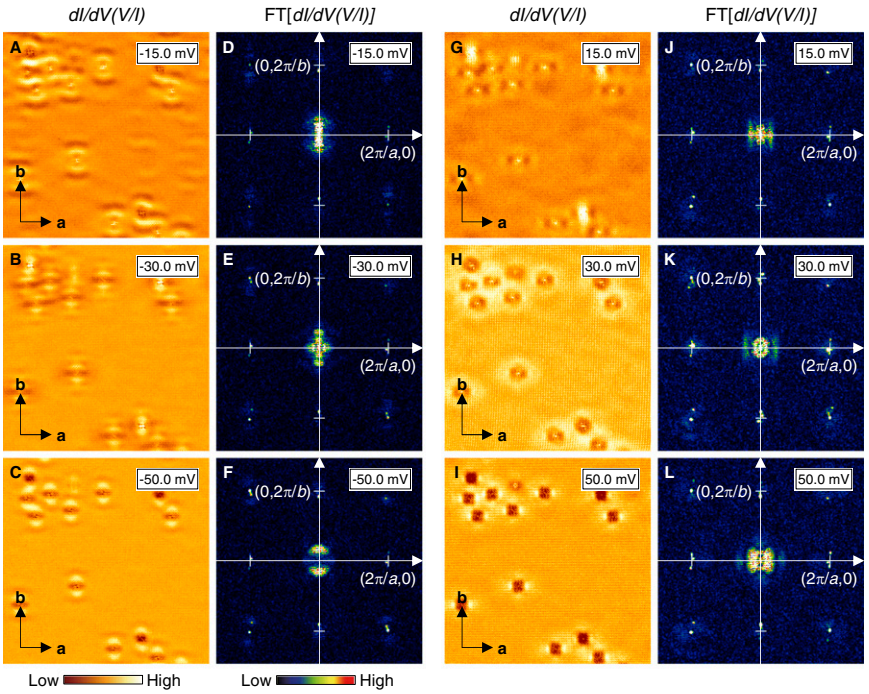

Fig. S5. Energy-dependent QPI patterns at $T = 1.5$ K and $\mu_0 H = 12$ T. Scan area is 45 nm×45 nm. Feedback conditions are $V_s = +50$ mV and $I_t = 100$ pA. Bias modulation amplitude for spectroscopy was set to 1 mV_{rms}. (*A–C*) Normalized conductance, *dI/dV(V/I)*, images of the occupied states at V = −15 mV (*A*), −30 mV (*B*), −50 mV (*C*). (*D–F*) Fourier transform of the images shown in *A–C*. (*G–I*) Normalized conductance images of the empty states at V = +15 mV (*G*), +30 mV (*H*), +50 mV (*I*). (*J–L*) Fourier transform of the images shown in *G–I*.

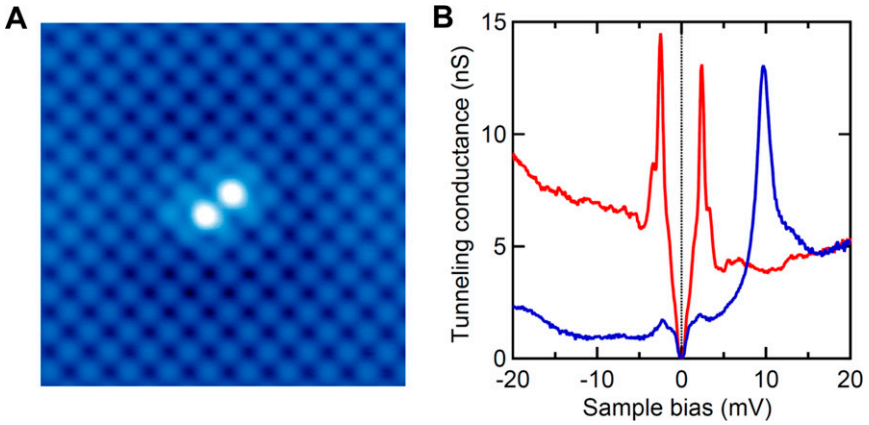

Fig. S6. Impurity states revealed by STM. (*A*) 5 × 5 nm^2 STM topographic image of the dumbbell-shaped impurity taken at $T = 0.4$ K. Feedback conditions are sample bias voltage $V_s = +95$ mV and tunneling current $I_t = 100$ pA. (*B*) Tunneling conductance spectra at $T = 0.4$ K. Spectra were taken with bias modulation amplitude 50 μV_{rms} after freezing the tip at $V_s = +20$ mV and $I_t = 100$ pA.

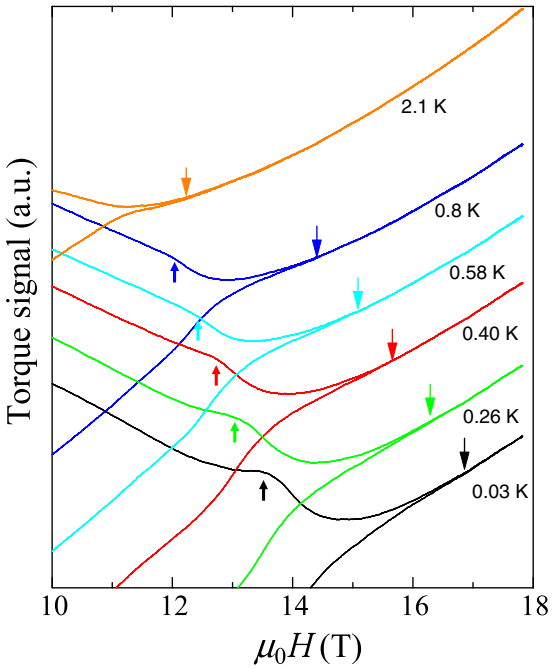

Fig. S7. Field dependence of the magnetic torque at low temperatures. Each curve is vertically shifted for clarity. Downward (upward) arrows mark the positions of the irreversibility (peak) field.